Chapter 5

Traveling Wave based Wide Area Backup Protection for HVAC network interfacing MMC based HVDC link

5.1 Introduction

5.1.1 General

The AC transmission lines and cables are generally exposed to disturbances, which can threaten the power system security unless protected by a robust transmission line protection scheme. It can be broadly classified into directional overcurrent, line differential and distance protection scheme, which are sensitive, selective and robust in nature. Out of this, the distance protection schemes are the most preferred option, which provides fast primary and slower backup protection for the HVAC transmission line. However, the conventional distance protection scheme may maloperate due to underreach, overreach, load encroachment and power swing which may lead to power system outages such as USA 2003 and India 2012 blackout [132, 133]. The modern day power system is evolving to a hybrid AC/DC grid, with integration of VSC based HVDC transmission system and renewable energy sources such as offshore wind farm to the conventional HVAC system [134]. The MMC, a type of VSC, is generally preferred for renewable energy integration, asyn-

chronous AC system interconnection and long distance power transfer capability.

5.1.2 Motivation and incitement

The grid fault characteristics of the hybrid AC/DC transmission system will be different from traditional HVAC grid, which can hinder the performance of conventional distance protection scheme. The integration of power electronics converter based renewable energy sources and HVDC transmission line leads to low short circuit ratio (SCR) of the hybrid AC/DC system [135], which will impact the behaviour of distance relaying scheme due to limited fault current from MMC converter [136]. The limited fault current and phase angle controlling capability of MMC converter may also impede the correct operation of distance protection scheme [137, 138]. Moreover, low inertia in a hybrid AC/DC system may lead to more frequency instability, incorrect memory polarization and remote infeed issues which can cause distance relay maloperation [139].

To independently regulate the transmitted reactive and active power, MMC uses constant AC/ DC voltage and constant active/reactive power control mode. As per the grid code requirement, during short circuit fault in AC line near point of common coupling (PCC) node, the reactive power control of MMC converter is activated to boost the PCC bus voltage. This is known as low voltage ride through (LVRT) control of MMC converter which supports the PCC bus voltage during short circuit event in HVAC grid. The impact of MMC's reactive power control on AC line voltage and current, and subsequently distance protection scheme, will be significant due to large sized MMC converter station of offshore wind farm or HVDC link [77]. Moreover, the positive sequence reactive current support by the MMC converter during unbalanced AC line fault will also modify the overall fault behavior compared to conventional synchronous generator (SG) based HVAC system, which in turn might effect the conventional distance relay operation [140, 141]. Another cause of concern with MMC interfaced HVAC system, is that the distance relay operations are sensitive to changes in AC voltage and active power reference setting of the MMC converter [142]. Therefore, it is quite prudent to study and develop a robust and secure protection scheme for HVAC grid considering effects of MMC interfaced HVDC transmission system.

5.1.3 Contribution

The main contributions of chapter are -

1. A novel secured TW based wide area backup protection scheme for mixed cable and overhead transmission line (OHTL) of AC grid interfacing MMC based HVDC link is designed, which is robust against MMC control schemes such as LVRT.

2. The fast successive matrix pencil algorithm (SMPA) and linear regression tool is used to extract TWAT information in the digital fault recorder (DFR) installed at the local terminal using low sampling frequency measurement (50 kHz). The extracted TWAT information will be sent as GOOSE message, defined by IEC-61850 communication standard, to the centralized wide area backup protection center (WABPC).

3. A graph theory-based real time fault location is calculated at the centralized WABPC using TWAT information received from distributed DFRs across HVAC system interfacing HVDC link. After that a wide area distance protection based supervisory trip signal is sent to assist the secured backup protection of HVAC grid against MMC control interference.

5.2 Proposed TW based WABPS for HVAC grid interfacing HVDC link

5.2.1 Low sampling frequency TW arrival time estimation

5.2.1.1 Pre-processing of relay input signal

To eliminate mutual coupling effect between measured three phase voltage signal, a modal transformation (Karenbauer transformation) equation is used prior to TW arrival time (TWAT) estimation as shown in (5.1) [89] -

$$\begin{bmatrix} u_\alpha \\ u_\beta \\ u_0 \end{bmatrix} = \frac{1}{3} \begin{bmatrix} 1 & -1 & 0 \\ 1 & 0 & -1 \\ 1 & 1 & 1 \end{bmatrix} \begin{bmatrix} u_a \\ u_b \\ u_c \end{bmatrix} \tag{5.1}$$

Here, u_α, u_β are aerial mode and u_0 is the ground mode voltage signal respectively, whereas u_a, u_b and u_c are the three phase AC voltage measured at the the DFRs located at transmission line or cable terminal end. Out of which, u_α (aerial mode signal) is selected as the relaying input signal for fault induced TWAT estimation.

5.2.1.2 Modified fast successive matrix Pencil algorithm (SMPA) based TWAT estimation

After modal transformation of the measured voltage signal, it is quite prudent to extract TWAT information from u_α using signal processing techniques. A band limited signal in a time period T, such as u_α, can be expressed as weighed summation of sinusoids or co-sinusoids using Fourier series as shown below -

$$u_\alpha(t) = \sum_{m=1}^{M} A_m \sin(2m\pi t/T + \phi_m) \tag{5.2}$$

Here M is the number of sinusoids along with residue $A_m \angle \phi_m$ required for reconstructing signal $u_\alpha(t)$. The more accurate representation of (5.2) can be expressed as weighed summation of damped sinusoids as shown below -

$$u_\alpha(t) = \sum_{m=1}^{M} A_m e^{-\alpha_m t} \sin(\omega_m t + \phi_m) \tag{5.3}$$

Where α_m (s^{-1}) and ω_m are the real part (damping factor) and imaginary part (angular frequency) of the m^{th} complex frequency $(\alpha_m \pm j\omega_m)$ component. Short time discrete Fourier transform (STDFT) is generally used for residue and frequency estimation for (5.2), whereas subspace based technique such as estimation of signal parameters via rotational invariant techniques (ESPIRIT) [143], matrix pencil algorithm (MPA) [128] and prony methods [144] are used for complex frequency and residue estimation for (5.3).

Since, MPA or any other subspace based method uses dual degree of freedom (damping factors and sinusoids) and DFT uses only sinusoids for signal reconstruction [145]. Therefore, MPA can reconstruct the pulse signal (TW) more effectively than DFT technique as evident from Fig. 5.1(a). The MPA method is applied to the TW samples inside a fixed size window, which slide along the time axis, and it is called successive MPA (SMPA) technique which extracts time-indexed complex frequency components as shown in Fig. 5.1(b). When the pulse signal (TW) enters the moving window, then the extracted damping factor (α) is positive, zero or negative depending on the position of TW in the

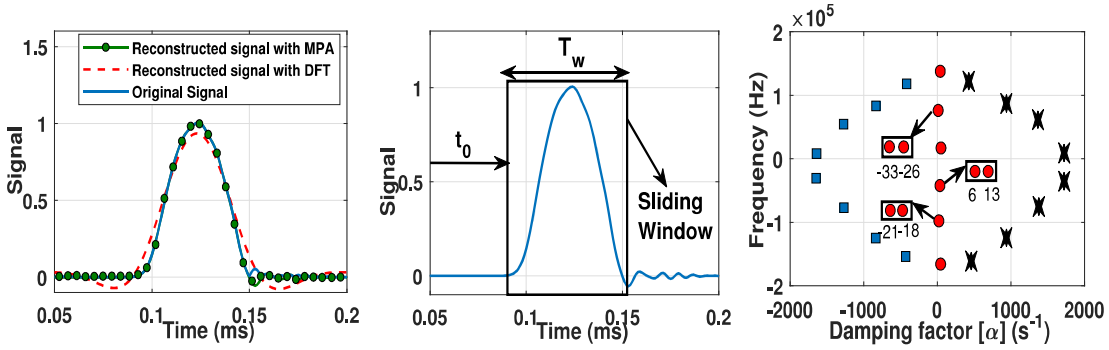

(a) (b) (c)

Figure 5.1: (a) Reconstructed pulse signal (TW) by SMPA and STDFT with the same number of terms of sinusoids. (b) Pulse-shape signal and sliding window. (c) Complex frequencies extracted by applying SMPA to the pulse shown in (b).

moving window. If TW enters from right side of the sliding window, then SMPA extracts positive α as shown in Fig. 5.1(c). As the position of pulse (TW) shifts toward middle of the window, then α value decreases gradually to zero value. With further movement of the sliding window, the pulse (TW) moves towards the left side of the moving window, and the extracted time-indexed damping factor (α) further decreases to negative value which is evident from Fig. 5.1(c). This principle can be used to extract arrival time (AT) of the TW (pulse), positioned as shown in Fig. 5.1(a), which can be mathematically written as [128] -

$$\alpha_m = 0, \forall m \rightarrow AT = t_0 + T_w/2 \tag{5.4}$$

Where α_m, AT, t_0 and T_w are the extracted damping factor, arrival time of the TW (pulse), position and width of the moving window respectively as described in Fig. 5.1(b).

For damping factor (α_m) extraction via fast SMPA method, a Hankel matrix $Y_{(N-L)X(L+1)}$ is formed using samples of u_α inside a N sample sized window, which is -

$$Y = \begin{pmatrix} u_\alpha(1) & u_\alpha(2)\cdots\cdots\cdots & u_\alpha(L+1) \\ u_\alpha(2) & u_\alpha(3)\cdots\cdots\cdots & u_\alpha(L+2) \\ \vdots & \vdots & \vdots \\ u_\alpha(N-L) & u_\alpha(N-L+1)\cdots & u_\alpha(N) \end{pmatrix} \tag{5.5}$$

Where $u_\alpha(.)$ and N represents aerial mode voltage signal sample value and number of signal samples inside the moving window respectively. The pencil parameter value (L) is advised to kept in between $N/2$ and $N/3$ for efficient noise filtration. Conventionally,

singular value decomposition (SVD), which is computationally expensive, is applied to matrix Y -

$$Y = USV^H \tag{5.6}$$

$$\sigma_s = 10^{-p}\sigma_{s\max} \tag{5.7}$$

Here, U, V are the unitary matrices, whose elements are eigen vectors of YY^H and Y^HY respectively. The S is a diagonal matrix which elements are the eigen value of Y and $(.)^H$ represents the complex conjugate operation on the matrix. In (5.6), the σ_s and $\sigma_{s\max}$ are the singular value elements and the largest singular value elements of matrix S. The parameter p is the filtering parameter which is used to separate signal and noise subspace matrices for further analysis.

The computational cost of MPA is mainly dominated by SVD, which can be replaced by the fast QR based decomposition algorithm along with low rank approximation [146]. The fast QR based decomposition algorithm will speed up calculation for (5.6) and principal component analysis (PCA) based pre-filtering [147] will help in faster noise cleaning effect for SVD based operation (5.7), which will further speed up the SMPA algorithm.

The summary of modified fast SMPA algorithm is described in Algorithm 1. An $(N-L)\times(L+1)$ sized initial Hankel matrix Y_0 is formed using mode-1 voltage sample u_α. In the next step, an auto-correlation matrix $B_x \approx \frac{1}{N-1}Y_0^TY_0$ is formulated. For filtering purpose, principle component analysis (PCA) is used on the covariance matrix B_x to find out its eigen decomposition matrix Γ instead of SVD based Cadzow method [147] which requires high computational burden. In step 3, $(.)^*$ denotes Hermitian transpose and the rank estimation is performed by counting the number of diagonal elements of Γ with normalized magnitude greater than ϵ. Compared to conventional PCA algorithm, additional steps are involved for reconstructing filtered and low rank Hankel matrix Y. To reconstruct the signal, elements among the anti-diagonal are averaged to preserve the Hankel structure for computational efficient QR decomposition [148]. To solve the general eigen value problem (GEP) in (5.6), SVDs are used in conventional MPA. In this chapter, a QR based GEP solver is embedded in SMPA for better computational efficiency as mentioned in step 8. In the next step, signal subspace and noise subspace are separated using filtering parameter described in (5.7). In step 10, matrix W and D are formulated by saving row of matrix $R\Pi^T$ and diagonal elements of R corresponding to dominant

singular value respectively. In step 11, T_0 and T_1 are formulated as -

$$\begin{aligned} T_0 &= D^{-1}W_l \\ T_1 &= D^{-1}W_r \end{aligned} \tag{5.8}$$

Where, W_l and W_r denotes the matrix obtained by deleting first and last column of W matrix respectively. After that, the eigen value of ${T_0}^+T_1$ ($(.)^+$ represent pseudo inverse operation) is used to find the complex frequencies of the windowed signal, as shown below -

$$\lambda_m = e^{(-\alpha_m \pm j\omega_m)T_s}, \forall m = 1, 2, 3.....n \tag{5.9}$$

Here, λ_m and T_s is the eigen value of ${T_0}^+T_1$ and sampling time period respectively. In the next step, the time indexed complex frequency is extracted using λ_m as shown below -

$$\alpha_m(t) \mp j\omega_m(t) = -\ln(\lambda_m)/T_s, \forall m = 1, 2, 3...n \tag{5.10}$$

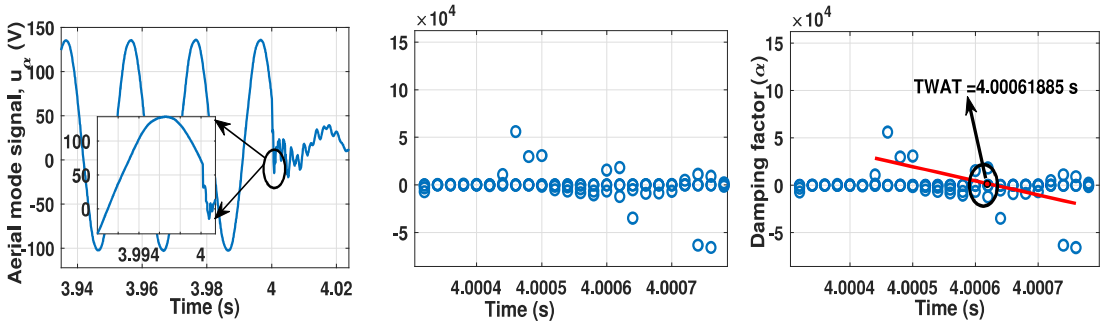

(a) (b) (c)

Figure 5.2: (a) Aerial mode voltage signal (u_α). (b) Damping factor-time diagram obtained by applying fast improved SMPA algorithm. (c) The fitted line to the dispersed damping factors (using linear regression), and its ZCP (TWAT) estimation.

The modified fast SMPA (with PCA based pre-filtering and QR based GEP), as mentioned in Algorithm 1, is used to extract time indexed damping factor (α_m) from the sliding window. For instance, the time indexed damping factor for the noise contaminated signal, shown in Fig. 5.2(a), is extracted using modified fast SMPA as shown in Fig. 5.2(b). The zero crossing point (ZCP) of α_m, shown in Fig. 5.2(b), is the TWAT as described in (5.4). But, the exact ZCP of α_m can not be calculated accurately. Therefore, linear regression tool is used for accurate estimation of the ZCP of α_m, where dispersed

Algorithm 1: Modified fast SMPA algorithm using PCA based pre-filtering and QR based GEP solver

PCA based pre-filtering$(\boldsymbol{u_\alpha(t), L, \epsilon})$

Step 1: Formulate initial Hankel matrix $\boldsymbol{Y_0}$ of size $(\boldsymbol{N-L}) \times (\boldsymbol{L+1})$.

Step 2: Compute $\boldsymbol{B_x} = \frac{1}{N-1}\boldsymbol{Y_0^T Y_0}$.

Step 3: Find $\boldsymbol{B_x} = \boldsymbol{X\Gamma X^*}$ using PCA. Columns of $\boldsymbol{Y}$ are eigen vectors of $\boldsymbol{B_x}$ and $\boldsymbol{\Gamma}$ is diagonal matrix of eigen values of $\boldsymbol{B_x}$.

Step 4: Find $\boldsymbol{Z} = \boldsymbol{rank(B_x)}$ by counting the number of eigen value with normalized magnitude $> \boldsymbol{\epsilon}$.

Step 5: Let $\tilde{\boldsymbol{X}}$ be the $\boldsymbol{Z}$ column of $\boldsymbol{X}$ and $\tilde{\boldsymbol{\Gamma}}$ be the diagonal matrix with first $\boldsymbol{Z}$ diagonal elements of $\boldsymbol{\Gamma}$.

Step 6: Compute $\tilde{\boldsymbol{Y_0}} = \boldsymbol{Y_0}\tilde{\boldsymbol{X}}\tilde{\boldsymbol{X}}^*$.

Step 7: Matrix $\boldsymbol{Y}$ is obtained by averaging anti diagonal elements of matrix $\tilde{\boldsymbol{Y_0}}$.

return $(\boldsymbol{Y})$

QR based GEP solver$(\boldsymbol{Y, L, p})$.

Step 8: Compute column-pivoted QR decomposition: $\boldsymbol{Y\Pi = QR}$ (Here, $\boldsymbol{\Pi}$ is a permutation matrix).

Step 9: Find $\boldsymbol{Z} = \boldsymbol{Rank(B_x)}$ such that (5.7) is satisfied.

Step 10: Let $\boldsymbol{W}$ be the first $\boldsymbol{Z}$ row of matrix $\boldsymbol{R\Pi^T}$ and $\boldsymbol{D}$ be the diagonal matrix with first $\boldsymbol{Z}$ diagonal element of $\boldsymbol{R}$.

Step 11: Compute $\boldsymbol{T_0} = \boldsymbol{D^{-1}W_l}$ and $\boldsymbol{T_1} = \boldsymbol{D^{-1}W_r}$.

Step 12: Compute $\boldsymbol{A} = \boldsymbol{T_1^+ T_0}$.

Step 13: $\boldsymbol{\lambda}_m$ is the set of eigen value of matrix A.

return $(\boldsymbol{\lambda}_m)$

value of α_m is taken as independent variable and corresponding time is taken as dependent variable which is shown in Fig. 5.2(c).

$$\alpha_d(t) = a_0 + a_1 t + \varepsilon_d(t), \forall t \in (t_1, t_2), \forall m \tag{5.11}$$

Here t_1 and t_2 are the start and end timestamp of the dispersed time indexed damping factor α_d as shown in Fig. 5.2(c). a_1 (slope) and a_0 (constant) are the linear regression coefficient, whereas $\varepsilon_d(t)$ is the linear regression error term. The matrix form of (5.11) can be re-written as -

$$\alpha_d = t_d a + \varepsilon \tag{5.12}$$

Here $\alpha_d = [\alpha_m(t_1), ..., \alpha_m(t_2)]^T$ is the vector of time indexed dispersed damping factor, $a = [a_0, a_1]^T$ is the matrix of linear regression coefficient, $\varepsilon = [\varepsilon_d(t_1), ..., \varepsilon_d(t_2)]^T$ is the error vector and $t_d = \begin{bmatrix} 1.....1 \\ t_1.....t_2 \end{bmatrix}^T$ is the time vector. The regression coefficient of (5.12) can be calculated by solving -

$$\min_{a_0, a_1} (\alpha_d - t_d a) \tag{5.13}$$

The (5.13) can be solved as -

$$\hat{a} = (t_d^T t_d)^{-1} t_d^T \alpha_d \tag{5.14}$$

Where $\hat{a} = [\hat{a}_0, \hat{a}_1]^T$ is the estimated linear regression coefficient from (5.14) and $(.)^T$ is the matrix transposition operation. the ZCP (TWAT) of α_d can be estimated by solving $\hat{a}_0 + \hat{a}_1 t = 0$, as shown in Fig. 5.2(c), and given as -

$$TWAT = -\frac{\hat{a}_0}{\hat{a}_1} \tag{5.15}$$

5.2.2 TWAT based WABPS Using Graph Theory

In order to put forward the proposed TW based distance WABPS methodology, an undirected weighted graph network is used to represent the HVAC part of hybrid AC/DC transmission system. After that, two mathematical lemmas are presented. In addition, the TW arrival time equations are derived for faults at different points of the HVAC system. At last, the proposed TW based distance WABPS is presented.

5.2.2.1 Graph theory Representation of VSC Interfaced HVAC Grid

Any HVAC part of the hybrid AC/DC system can be represented by a un-directed weighted graph $g = (n, b, w)$, where $n = \{n_1, n_2, n_3, ...\}$, $w = \{w_1, w_2, w_3, ...\}$ and $b = \{b_1, b_2, b_3, ...\}$ are the set of nodes, weights and branches respectively. In a weighted graph g, $P^{min}_{n_1,n_2}$ is used to represent the shortest path between two nodes n_1 and n_2, which can also be represented as the set of all branches included in the path. Moreover, the distance between nodes n_1 and n_2 can be defined as sum of weights of branches involved in $P^{min}_{n_1,n_2}$ [149], which is denoted as D_{n_1,n_2}.

The weighted graph g is systematically sectionalize for wide area backup protection strategy using two lemmas, whose associated proofs are provided in the Appendix B, which are -

Lemma I : If a point f lies on the shortest path between two arbitrary nodes n_1 and n_2 on the graph g, then this path can be represented as the union of the shortest path between node n_1 and f, and the one between f and n_2.

Lemma II : Assuming a branch between nodes n_1 and n_2, i.e..; $(n_1, n_2) \in b$. For any shortest path between nodes n_2 and n_3 passes through node n_1, then for any random point f on the branch (n_1, n_2), the node n_1 must lie on the shortest path between f and n_3.

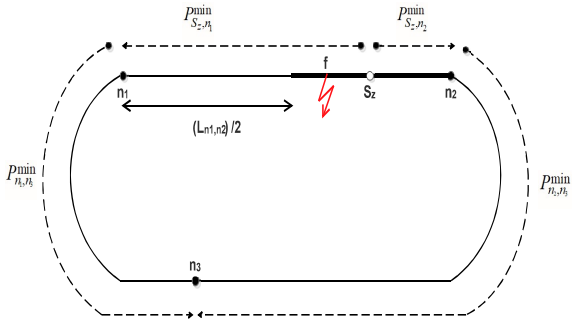

Figure 5.3: Locus of symmetric point S_z in graph G.

The fault induced TW will always travel the shortest path from the fault point to the transient detector location. The TW velocity in each branch (transmission line/cable), (n_1, n_2), is denoted by v_{n_1,n_2}. Depending on the material and geometry of the conductor of transmission line/cable (branch), the TW velocity will be different in each branch. Therefore, to make the fault induced TWAT at each detector to be directly proportional to the distance between the fault point and the detector, the weight of each branch (n_1, n_2) of graph g is multiplied by $v_0/v_{n_1,n_2}$, where v_0 is the base TW velocity. Suppose a line with

different segments connects two nodes n_1 and n_2, and a detector is located at terminal n_3 as shown in graph representation in Fig. 5.3. The shortest path and distance from the fault point f to transient detector location n_3 is calculated as -

$$\begin{aligned} P^{min}_{f,n_3} &= min(P^{min}_{f,n_1} \cup P^{min}_{n_1,n_3}, P^{min}_{f,n_2} \cup P^{min}_{n_2,n_3}) \\ D_{f,n_3} &= min(D_{f,n_1} \cup D_{n_1,n_3}, D_{f,n_2} \cup D_{n_2,n_3}) \end{aligned} \tag{5.16}$$

Without any loss of generality, it is assumed that the D_{n_1,n_3} is shorter than or equal to D_{n_2,n_3}. Considering the path between n_2 and n_3, which passes through the node n_1 as an upper boundary for $P^{min}_{n_2,n_3}$, the constraint for D_{n_2,n_3} would be -

$$D_{n_1,n_3} \leq D_{n_2,n_3} \leq D_{n_2,n_2} + D_{n_1,n_3} \tag{5.17}$$

The conditions under which both the values in (5.16) are equal and S_z be the symmetric point between P_{n_1,n_2}, which hold equality constraint condition. By equating this two values -

$$D_{S_{n_3},n_1} = \frac{D_{n_2,n_3} - D_{n_1,n_3} + D_{n_2,n_1}}{2} \tag{5.18}$$

The symmetric point S_{n_3}, whose shortest distances from node n_3 exist in two possible directions, one traverses through node n_1 and another through n_2, which can be determined from (5.17) and (5.18). As per *Lemma II*, the shortest path from each arbitrary point f on segment (S_{n_3}, n_1) to the node n_3 would surely contains node n_1. Similarly, the shortest path between any arbitrary point f on line segment (S_{n_3}, n_2) to node n_3 would pass through the node n_2.

let's assume I to be a set having indices of all nodes equipped with transient detector (DFR). Suppose for branch (n_1, n_2), the symmetric point S_{n_3} is found for detector at node $n_3 \in I$, then the branch (n_1, n_2) will be sectionalized into at most $|I| + 1$ segments. Here, $|I|$ represents the number of elements in the sets, i.e.; also known as cardinality of I. Therefore, for any fault point f on the line segment (n_x, n_y), it is pre-decided whether the shortest path will traverse the node n_1 or n_2, and it is to be noted that this property is independent on the location of f on the (n_x, n_y) segment. It can be finally concluded that, the first detected TW surge traversal node, either n_1 or n_2, for any fault point f on branch (n_1, n_2) can be determined, if the fault segment is determined.

The wide area backup protection strategy involves mainly two stages at the centralized location. First, the fault equations associated line sections of the sectionalized

graph network is derived and an algorithm is proposed to identify the faulted segment. In second stage, the relevant system of fault equation are solved to calculate real time fault location for wide area distance based protection and it sends an appropriate backup trip signal to the associated circuit breaker.

5.2.2.2 Fault Equations for Different Segments of VSC Converter Interfaced HVAC System

Assuming appropriate sectionalization of the graph g with respect to TW detector location as explained before. Let $(n_x, n_y$ be the line segment on the branch (n_1, n_2) of graph g, and $I_{n_1}^{(n_x,n_y)}$ & $I_{n_2}^{(n_x,n_y)}$ are the sets of all detectors where the TW surge emanating from f on segment (n_x, n_y) traverses through node n_1 and n_2 in their path respectively. It can also be mentioned that -

$$I_{n_1}^{(n_x,n_y)} \cup I_{n_2}^{(n_x,n_y)} = I \tag{5.19}$$

The following two group of TWAT equations can be formulated -

$$\begin{aligned} t_i^{AT} &= t_0 + \frac{D_{f,n_1}}{v_0} + \frac{D_{n_1,i}}{v_0}, \forall i \in I_{n_1}^{(n_x,n_y)} \\ t_i^{AT} &= t_0 + \frac{D_{f,n_2}}{v_0} + \frac{D_{n_2,i}}{v_0}, \forall i \in I_{n_2}^{(n_x,n_y)} \end{aligned} \tag{5.20}$$

Where, t_i^{AT} is the first TWAT at detector location i. It can be further deduced that $L_{n_1,n_2} = D_{f,n_1} + D_{f,n_2}$, as the fault point f lies on the line/branch (n_1, n_2). There are also some topology dependent parameters, such as $T_{n_1,n_2} = L_{n_1,n_2}/v_0$, $T_{n_2,i} = D_{n_2,i}/v_0$ and $T_{n_1,i} = D_{n_1,i}/v_0$. And the unknown term $D_{n_1,f}/v_0$ in (5.20) is expressed as t_{f,n_1} and the rewritten set of equations are -

$$\begin{aligned} t_i^{AT} - T_{n_1,i} &= t_0 + t_{f,n_1}, \forall i \in I_{n_1}^{(n_x,n_y)} \\ t_i^{AT} - T_{n_2,i} - T_{n_1,n_2} &= t_0 - t_{f,n_1}, \forall i \in I_{n_2}^{(n_x,n_y)} \end{aligned} \tag{5.21}$$

To solve (5.21), the shortest path and the distance between all node pairs (all $D'_{n_1,n_2}s$) need to found first, which can be achieved using the efficient algorithm proposed in [150]. The (5.21) can be further simplified in the matrix form as -

$$N = \begin{bmatrix} H_{n_1}^{(n_x,n_y)} \\ H_{n_2}^{(n_x,n_y)} \end{bmatrix} \times \begin{bmatrix} t_0 \\ t_{f,n_1} \end{bmatrix} \tag{5.22}$$

Where N is a measurement matrix of size $(|I|_{n_1}^{(n_x,n_y)} + |I|_{n_2}^{(n_x,n_y)})X1$ and the $H_{n_1}^{(n_x,n_y)}$

& $H_{n_2}^{(n_x,n_y)}$ are -

$$H_{n_1}^{(n_x,n_y)} = \begin{bmatrix} 1 & 1 \\ \vdots & \vdots \\ 1 & 1 \end{bmatrix}_{\left|I_{n_1}^{(n_x,n_y)}\right|\times 2}$$

And,

$$H_{n_2}^{(n_x,n_y)} = \begin{bmatrix} 1 & -1 \\ \vdots & \vdots \\ 1 & -1 \end{bmatrix}_{\left|I_{n_1}^{(n_x,n_y)}\right|\times 2}$$

(5.22) is the set of two linear equations with two unknown variables (inception time and real time fault distance), which can be solved using least square technique for the fault f on line segment (n_x, n_y). Finally, the real time fault distance on transmission line (branch) (n_1, n_2) is calculated as $v_{n_1,n_2} \cdot t_{f,n_1}$, where v_{n_1,n_2} is the TW velocity in branch (n_1, n_2)

5.2.2.3 Fault Segment Identification for WABPS

A wide area real time fault distance is calculated by solving (5.22) for a fault on the line segment on sectionalized graph g. But, the faulted segment is not known prior to solving (5.22). Therefore, the faulted line segment is identified by subtracting all possible equations pair in (5.21) as shown below -

$$\begin{aligned} t_i^{AT} - t_j^{AT} &= T_{n_1,i} - T_{n_1,j}, \forall i,j \in I_{n_1}^{(n_x,n_y)} \\ t_i^{AT} - t_j^{AT} &= T_{n_2,i} - T_{n_2,j}, \forall i,j \in I_{n_2}^{(n_x,n_y)} \end{aligned} \tag{5.23}$$

It can be pointed out that the AT difference between specified detector pair i and j is not dependent on line segment (n_x, n_y). Therefore, for all line segment (n_x, n_y) located on branch (n_1, n_2), the following equations is constituted for TWAT at different detector location -

$$\sum_{\forall i,j \in I_{n_1}^{(n_x,n_y)}} \left|(t_i^{AT} - t_j^{AT}) - (T_{n_1,i} - T_{n_1,j})\right| + \sum_{\forall i,j \in I_{n_2}^{(n_x,n_y)}} \left|(t_i^{AT} - t_j^{AT}) - (T_{n_2,i} - T_{n_2,j})\right| \tag{5.24}$$

As per (5.23), if fault is on line segment (n_x, n_y), then (5.24) would be equal to zero, maybe small positive number due to rounding off error and measurement errors. hence,

the faulted line segment is identified, which is prerequisite for identifying real time fault distance in WABPS.

5.2.3 Proposed TW based WABPS

Based on aforementioned explanation for modified fast SMPA & linear regression tool based low sampling frequency TWAT estimation and graph theory based wide area fault localization technique, a robust TW based WABPS is proposed for HVAC grid interfacing with MMC based HVDC transmission line It requires two stages -

Offline Stage:

1. The graph topology of the HVAC part of the hybrid AC/DC grid is derived, which is generally fixed.

2. Considering the location of fault detector (digital fault recorder (DFR)), all branches of the derived graph topology are sectionalized using (5.18). After that, a set B^{new} is formed containing all segments whose terminal ends are either node or symmetrical nodes on the branch.

3. For all segment, i.e.; $\forall(n_x, n_y) \in B^{new}$, with respect to the branch under study say (n_1, n_2), the set I_{n1} and I_{n2} are obtained as explained in previous section.

Online Stage (WABPS):

1. The TWAT due to fault induced TW is estimated at different digital fault detector location across HVAC side of the hybrid AC/DC system using modified fast SMPA and linear regression tool using low sampling frequency (50 kHz) measurements.

2. For all offline identified segments, i.e.; $\forall(n_x, n_y) \in B^{new}$, (5.24) is calculated. The line segment whose evaluated value is lowest among all would be considered as the faulted segment.

3. In the next step, the system of equations (5.21) for the identified line segment, in previous step, is solved to estimate real time wide area based fault location, which is used to send backup trip signal to the associated circuit breaker (CB) for secured zone- 2 or 3 backup protection.

5.3 Test hybrid AC/DC system

To evaluate the performance of proposed TW based WABPC, a test hybrid AC/DC transmission system is modeled as shown in Fig. 5.4(a). It consist of two half bridge MMC converters (MMC 1 and MMC 2), inter connecting two AC grid via DC transmission line parallel to AC transmission line, in a symmetrical monopolar configuration with LVRT capability. The detailed description of the MMC converters and hybrid AC/DC grid parameters are tabulated in Table 5.1.

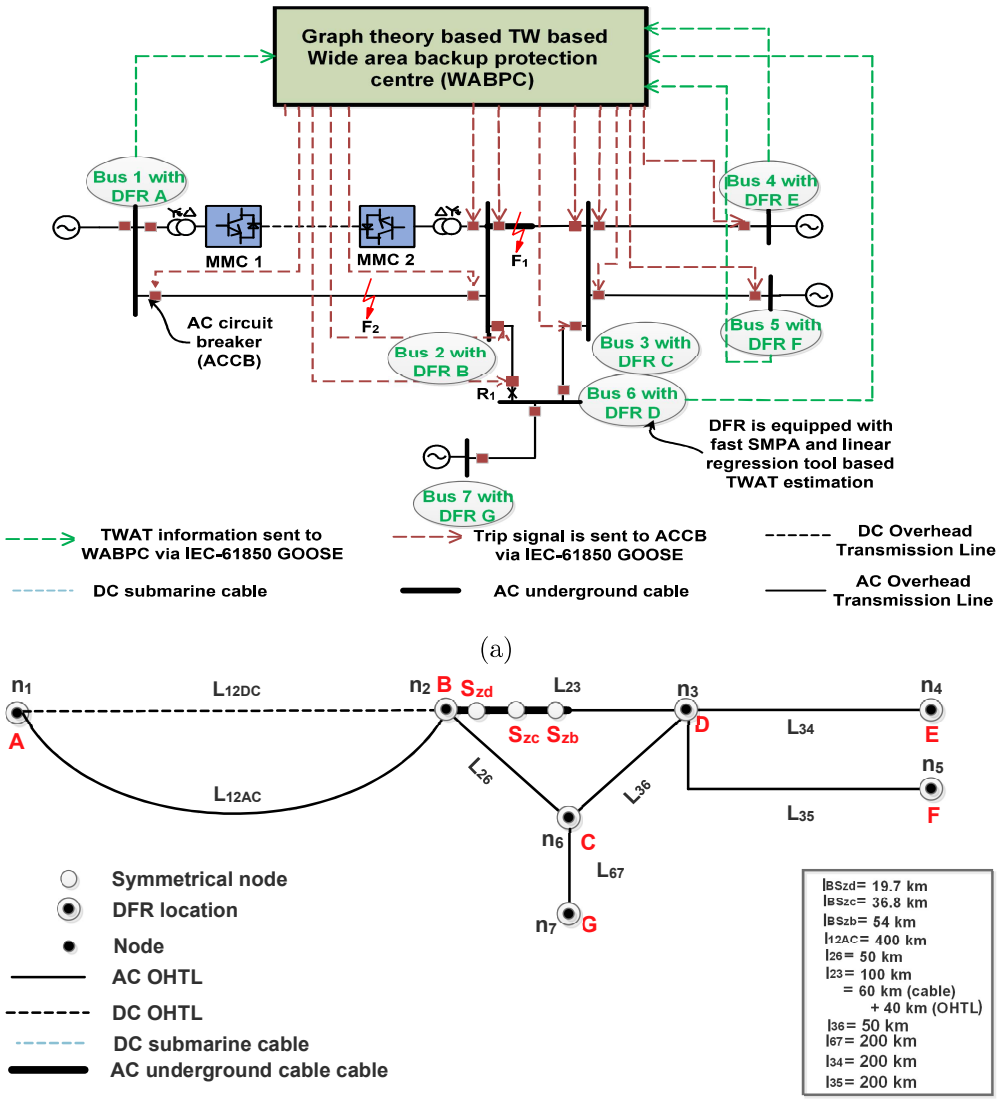

Figure 5.4: (a) Schematics of proposed WABPS for test hybrid AC/DC grid interfacing offshore wind farm. (b) Associated sectionalized graph representation.

Table 5.1: MMC converters and AC/DC grid parameters

Converter and grid parameters	Converter 1	Converter 2
Rated power (MVA)	1500	1500
AC grid voltage (kV)	400	400
DC grid voltage (kV)	± 320	± 320
Control mode	V_{AC} and V_{DC}	P and Q
AC converter ratio (Grid/VSC)	400/175	400/175
Frequency (Hz)	50	50
Arm capacitance (μF)	33.5	33.5
Arm reactor (mH)	50	50
Arm resistance (Ω)	0.385	0.385
Bus filter reactor (mH)	15	15

The digital fault recorder (DFR) with IEC-61850 communication protocol capability is installed at AC buses as shown in Fig. 5.4(a), which is equipped with modified fast SMPA and linear regression based TWAT estimation tool requiring low sampling frequency measurement (50 kHz). For fault F_1 and F_2 in the test hybrid AC/DC grid shown in Fig. 5.4(a), the time synchronized TWAT information extracted at the installed DFRs are transferred to the graph theory based centralized WABPC via dedicated communication channel conforming to IEC-61850 GOOSE message protocol. The graph theory based TW equations (5.24) and (5.21) are used to identify the real time faulted segment and accurate fault location in a hybrid AC/DC transmission system and CB trip signal is sent to the associated AC circuit breaker (ACCB) unit using IEC-61850 GOOSE message for resilient backup protection of HVAC grid against MMC converter control interference. The sectionalized graph theory representation of the test hybrid AC/DC transmission system is drawn in Fig. 5.4(b), which shows the symmetrical node and DFR locations in graph network of the test hybrid AC/DC system. In order to investigate the performance of proposed TW based WABPS, a complex meshed and radial hybrid AC/DC grid with mixed cable and overhead transmission line is considered in the test hybrid AC/DC system. As clear from Fig. 5.4(b), the symmetrical nodes for node "B", "C" and "D"

are S_{zb}, S_{zc} and S_{zb} respectively. The location of S_{zb}, S_{zc} and S_{zb} from AC bus B are 54 km, 36.8 km and 19.7 km respectively, which is calculated using (5.18). The symmetrical nodes for node B and D lies in L_{23}, instead of L_{26} and L_{36}, due to traveling wave velocity parity between short length cable and OHTL. Therefore, symmetrical nodes S_{zb} and S_{zb} are redundant and only S_{zc} will be considered for sectionalizing line L_{34} in two sections $L_{B,S_{zc}}$ and $L_{S_{zc},D}$.

5.4 Simulation results and discussion

The hybrid AC/DC transmission system shown in Fig. 5.4 is modeled in PSCAD/EMTDC software. The half bridge MMC (HBMMC) converter model is developed using continuous equivalent MMC model with blocking/de-blocking capability. For accurate transient behavior of hybrid AC/DC transmission system, the overhead transmission line (OHTL) and cable are modeled using frequency dependent (phase) models. The TW velocity for the cable and OHTL is found to be 121.30 km/ms and 355.219 km/ms respectively. The MMC converter's internal overvoltage and overcurrent protection triggers blocking signal of IGBTs to protect MMC converter circuit. The simulation time step is selected as 20 μs corresponding to 50 kHz sampling frequency measurement and signal-to-noise- ratio is considered to be 50 dB, unless stated otherwise.

5.4.1 Impact of fault location

To study the impact of fault location on the proposed TW based wide area backup protection scheme, a three phase (LLL) fault is simulated at F_1 with varying fault distance in AC cable and OHTL between AC bus 2 and 3 as shown in Fig. 5.4(a). At first, the fault location is set at 48 km from AC bus 2 in cable part of the mixed cable/OHTL between AC bus 2 and 3 in test hybrid AC/DC system. The SMPA based algorithm employed inside the DFRs installed at the AC buses are shown in Fig. 5.5. The extracted TWATs at all 7 DFRs for fault induced TW are sent to WABPC, where graph theory algorithms are used to identify the fault segment and real time fault localization. (5.24) is used to identify (coarse estimation) the faulted segment in the HAVC network, whereas (5.22) is used to estimate the real time fault location. If the calculated fault location (CFL) falls in the protected zone for zone-2 and zone-3 of assumed relay location R_1, then a supervisory

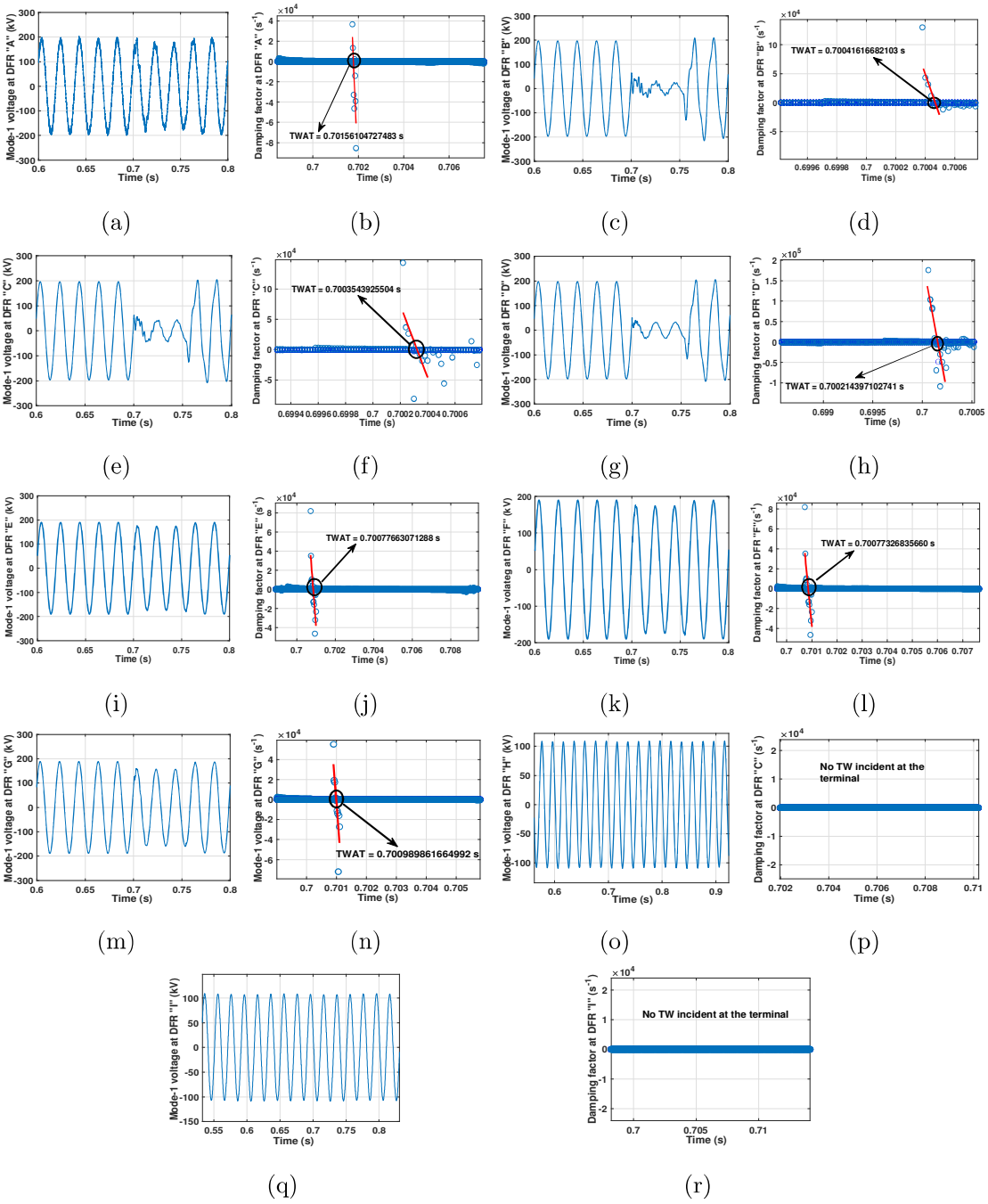

Figure 5.5: SMPA performance (a) u_α at DFR "A", (b) TWAT at DFR "A", (c) u_α at DFR "B", (d) TWAT at DFR "B", (e) u_α at DFR "C", (f) TWAT at DFR "C", (g) u_α at DFR "D", (h) TWAT at DFR "D", (i) u_α at DFR "E", (j) TWAT at DFR "E", (k) u_α at DFR "F", (l) TWAT at DFR "F", (m) u_α at DFR "G", (n) TWAT at DFR "G", (o) u_α at DFR "H", (p) TWAT at DFR "H", (q) u_α at DFR "I", (r) TWAT at DFR "I".

trip signal is sent to assist secured backup protection of HVAC grid.

Similarly, the TWATs estimated using fast modified SMPA algorithm at 7 DFRs location in test system is tabulated in Table 5.2 for 48 km, 20 km, 10 km, 30 km and 50 km fault location from AC bus 2. As evident from Table 5.2, the TW based wide area real time fault location is estimated using graph theory tool and the maximum fault location error (FLE) (4.13) comes out to be 0.132 % . It also correctly identifies the fault zone for Relay R_1 (Zone 1 - 40 km (80 % of L_{26}), Zone 2 - 60 km (120 % of L_{26}) and Zone 3 - 450 km(100 % of L_{26}+100 % of L_{12AC})) as observed in Table 5.2 for fault F_1.

Table 5.2: Performance of proposed WABPS for different fault location in L_{23} (Fault distance is calculated from Bus 2)

Fault	TWAT at DFR location							Fault	FLE
distance (km)	DFR A	DFR B	DFR C	DFR D	DFR E	DFR F	DFR G	zone	(%)
48	0.701561047	0.700416167	0.700354393	0.700214397	0.700776631	0.700773268	0.700917837	Zone-3	0.068
20	0.701297261	0.700165831	0.700308482	0.700445831	0.70100817	0.7010008541	0.700865567	Zone-3	0.101
10	0.701210296	0.700082739	0.700227394	0.700364927	0.700930359	0.700927932	0.700786831	Zone-2	0.03
30	0.701376721	0.700250264	0.700386829	0.700361429	0.700921886	0.700926397	0.700953387	Zone-3	0.132
55	0.701602954	0.700477531	0.700338550	0.700192853	0.7007581174	0.7007848230	0.700899590	Zone-3	0.051

5.4.2 Impact of fault impedance

To study the impact of fault impedance on the performance of proposed WABPS, a single phase to ground (LG) F_1 with fault impedance of 20 Ω, 60 Ω and 100 Ω is simulated in L_{23} at a distance of 30 km from AC bus 2 (Node "B") in the test hybrid AC/DC system. The fast SMPA algorithm's performance is evaluated at DFR "B" in Fig. 5.6, where the estimated TWAT is 0.7002473170 s, 0.700247016 s and 0.700246932 s for 20 Ω, 60 Ω and 100 Ω respectively. It is clear from Fig. 5.6 that the effect of fault type has non-significant effect on proposed fast SMPA's algorithm accuracy for fault resistance up to 100 Ω. Concurrently, the extracted TWAT for other DFRs are estimated and tabulated in Table 5.3 and (5.24) & (5.22) of the graph theory algorithm is used to identify the fault zone and fault location. The identified fault zone (zone -3) is accurate which ensures secured backup protection for the mixed cable and OHTL in HVAC grid. Similarly, different combination of fault resistance and fault location are simulated in test hybrid AC/DC system and its performance is tabulated in Table 5.3 which verifies that the proposed WABPS is robust and secure.

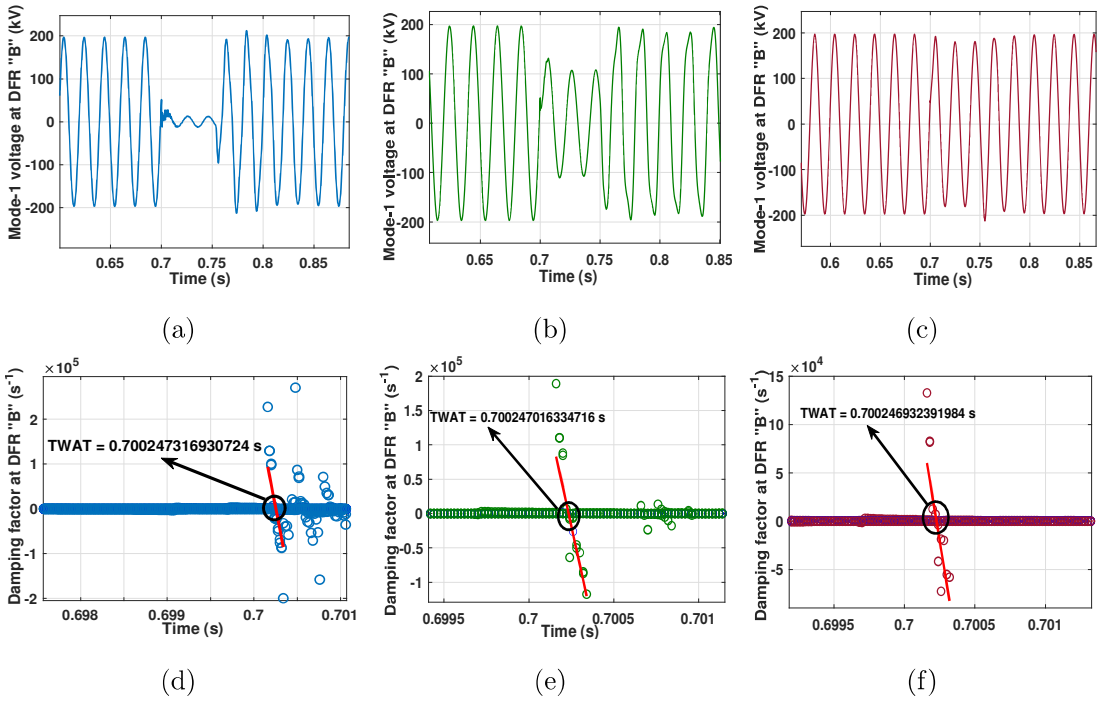

Figure 5.6: Impact of fault impedance on the proposed fast SMPA based TWAT estimation (a) TWAT at DFR "B" for 20 Ω fault resistance, (b) TWAT at DFR "B" for 60 Ω fault resistance, (c) TWAT at DFR "B" for 100 Ω fault resistance.

Table 5.3: Performance of wide area protection scheme for different fault location and fault impedance on transmission line and cable in L_{23} (Fault distance is calculated from Bus 2)

Fault resistance (Ω) & distance (km)	TWAT at DFR location							Fault zone	FLE (%)
	DFR A	DFR B	DFR C	DFR D	DFR E	DFR F	DFR G		
20 & 30	0.7013734120	0.7002473170	0.700388152	0.700359965	0.700923953	0.700920940	0.700953032	Zone-3	0.125
60 & 30	0.701372792	0.700247016	0.700387790	0.700356043	0.700922017	0.700920069	0.7009555202	Zone-3	0.105
100 & 30	0.7013744159	0.700246932	0.700388208	0.700359821	0.700921930	0.700922081	0.700951106	Zone-3	0.111
20 & 80	0.701453039	0.700337915	0.700197793	0.70005530	0.700620338	0.70061940	0.700762729	Zone-3	0.189
60 & 80	0.7014543755	0.7003350942	0.70019829	0.700057209	0.700619950	0.700622865	0.700760369	Zone-3	0.192
100 & 80	0.7014552350	0.700334820	0.700199202	0.700056320	0.7006179290	0.700619022	0.700757037	Zone-3	0.206

5.4.3 Impact of fault type

In this subsection, the effect of fault type is initially studied on the accuracy of proposed SMPA algorithm by simulating line-to-ground (LG) fault, line-to-line (LL) fault and three phase or line-line-line (LLL) fault F_1 in transmission line at 30 km distance from node B

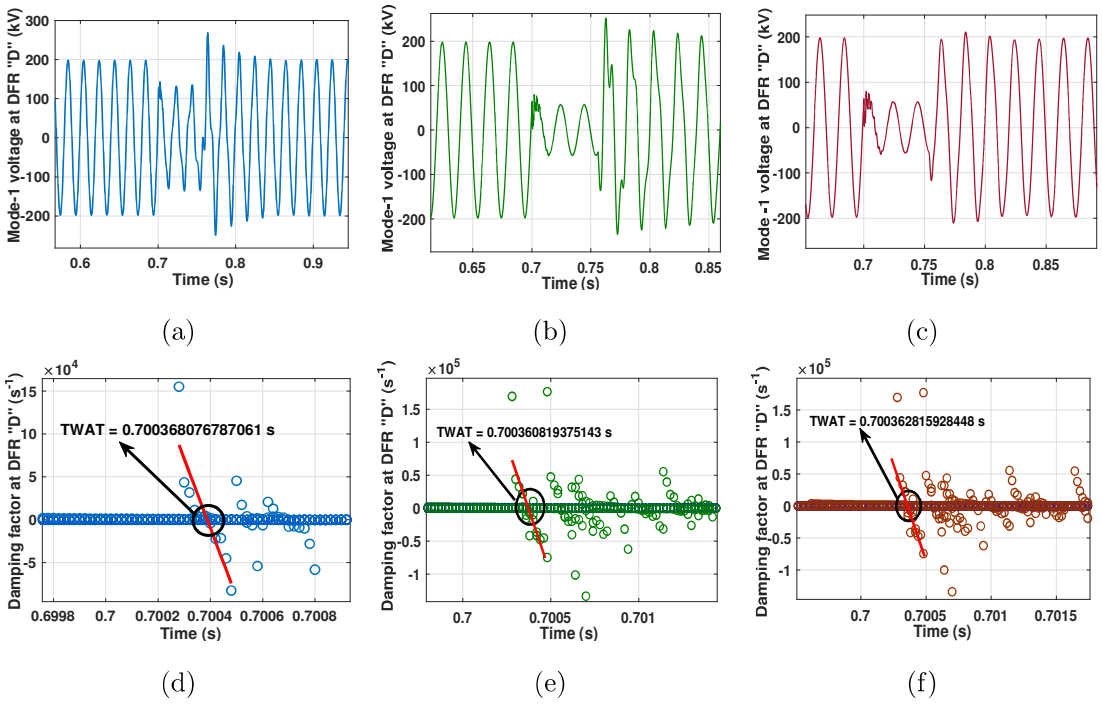

Figure 5.7: Impact of fault type on the proposed fast SMPA based TWAT estimation (a) TWAT at DFR "D" for LG fault type, (b) TWAT at DFR "D" for LL fault type, (c) TWAT at DFR "D" for LLL fault type.

in cable between node B and D. The extracted TWAT is 0.700368071 s, 0.700360819 s and 0.700360281 s for LG, LL and LLL fault respectively as shown in Fig. 5.7, which indicates that the proposed TWAT estimation technique is robust against fault types. To further evaluate the performance of proposed graph theory based WABPS, the estimated TWAT at other DFRs for LG, LL and LLL fault are tabulated in Table 5.4. (5.24) and (5.22) are used to locate fault and identify the fault zone for relay R_1, which comes out to be zone-3. Similarly, other fault location and types are simulated in a test hybrid AC/DC grid and its performance is tabulated in Table 5.4, which verifies that the proposed WABPS is insensitive to different fault type.

5.4.4 Impact of time synchronization error

The accuracy of TWAT estimation relies heavily on the precise synchronization of measurements at the AC bus (DFR location). Any deviation in estimated TWAT at different DFR location due to time synchronization error (TSE) might lead to significant error in

Table 5.4: Performance of wide area protection scheme for different fault location and fault type in L_{23} (Fault distance is calculated from Bus 2)

Fault type & distance (km)	TWAT at DFR location							Fault zone	FLE (%)
	DFR A	DFR B	DFR C	DFR D	DFR E	DFR F	DFR G		
LG & 30	0.701372907	0.7002457251	0.700390633	0.700368071	0.700922910	0.700920773	0.700950927	Zone-3	0.257
LL & 30	0.701373229	0.700246123	0.700389384	0.700360819	0.700925847	0.700923184	0.700953602	Zone-3	0.145
LLL & 30	0.701354295	0.700245841	0.700388375	0.700360281	0.700922494	0.700922297	0.700951593	Zone-3	0.168
LG & 50	0.701538524	0.700414294	0.700337063	0.700195749	0.700760015	0.700758502	0.700900140	Zone-3	0.184
LL & 50	0.701537739	0.700412407	0.700336306	0.700194478	0.700759069	0.7007581155	0.700899037	Zone-3	0.183
LLL & 50	0.701538629	0.7004143970	0.7003372290	0.700195296	0.700760649	0.700758013	0.700899045	Zone-3	0.177

estimated real time fault location and incorrect distance relay zone identification. The proposed WABPS uses IEC-61850 communication protocol which is integrated with IEEE-1588 precision time protocol (PTP) for precise time synchronization within 30 - 50 ns among IEC-61850 enabled DFRs [105]. A time synchronization error (Δt_{syn}) of 3 μs and 5 μs is considered for a fault in AC transmission line L_{23} and its performance is evaluated and tabulated in Table 5.5. As clear from Table 5.5, the estimated fault location and identified fault zone is least affected by TSE up to 5 μs which indicates its robustness against time synchronization error.

Table 5.5: Performance of proposed WABPS for different time synchronization error in L_{23} (Fault distance is calculated from Bus 2)

Fault distance (km) & TSE (μs)	TWAT at DFR location							Fault zone	FLE (%)
	DFR A	DFR B	DFR C	DFR D	DFR E	DFR F	DFR G		
48 & ± 0	0.701561047	0.700416167	0.700354393	0.700214397	0.700776631	0.700773268	0.700917837	Zone-3	0.068
48 & ± 3	0.701564047	0.700419167	0.700357393	0.700217397	0.700779631	0.700776268	0.700920837	Zone-3	0.152
48 & ± 5	0.701611047	0.700421167	0.700359393	0.700219397	0.700781631	0.700778268	0.700922837	Zone-3	0.272
30 & ± 0	0.701376721	0.700250264	0.700386829	0.700361429	0.700921886	0.700926397	0.700953387	Zone-3	0.132
30 & ± 3	0.703709721	0.700253264	0.700389829	0.700364429	0.700924886	0.700929397	0.700956387	Zone-3	0.180
30 & ± 5	0.701381721	0.700255264	0.700391829	0.700366429	0.700926886	0.700931397	0.700958387	Zone-3	0.321

5.4.5 Impact of fault inception angle

The accuracy of TWAT estimation depends on the fault inception angle (FIA) which influences the traveling wave-shapes and therefore it impacts the performance of TW based

protection and fault localization scheme. In this section, the performance of proposed TWAT based wide area backup protection and fault localization scheme is validated for different fault inception angle. The fault is incepted in transmission line L_{23} at 80 km with fault resistance varying from 10 Ω to 100 Ω whereas fault inception angle (FIA) is varied from 0° to 90°. The performance of the proposed scheme is tabulated in Table 5.6 and it can be summarized that the performance of proposed TWAT based WABPS is resilient to fault inception angle parameter.

Table 5.6: Performance of proposed WABPS for different FIA in L_{23} (Fault distance is calculated from Bus 2)

Fault resistance	TWAT at DFR location							Fault	FLE
(Ω) & FIA (°)	DFR A	DFR B	DFR C	DFR D	DFR E	DFR F	DFR G	zone	(%)
10 & 0	0.7014530391	0.7003350942	0.70019829	0.700057209	0.700619950	0.700622865	0.700760369	Zone-3	0.192
10 & 60	0.70145296381	0.70033353213	0.7001993522	0.7000573721	0.7006200284	0.70062539228	0.7007619462	Zone-3	0.252
10 & 90	0.70145316634	0.70033549361	0.70019749251	0.70005578252	0.70061987243	0.70062578245	0.7007597264	Zone-3	0.294
100 & 0	0.70145398521	0.70033503723	0.70019927640	0.70005629612	0.70061768421	0.70062337154	0.70076196236	Zone-3	0.249
100 & 60	0.70145447238	0.70033189521	0.70019937260	0.70057084728	0.70062286002	0.70062510627	0.70076228551	Zone-3	0.172
100 & 90	0.7014527401	0.70033724952	0.700196902521	0.7000584921	0.7006199729	0.7006259342	0.7007608723	Zone-3	0.489

5.4.6 Impact of LVRT control of MMC converter

There will be an impact of LVRT controller of MMC converter on the apparent impedance seen by the conventional distance (mho) relay, which is given as [140] -

$$Z_{app}^{AG} = \frac{(Res_F + pZ_L^1)I_{R_1}^a + Res_f I_{grid}^a + 3pZ_L^1 I_{tr}^0}{I_{R_1}^a + 3kI_{tr}^0} \tag{5.25}$$

Where Z^{AG}, Res_F, p, Z_L^1, $I_{Res_A}^a$, I_{grid}^a, I_{tr}^0 and k are the apparent fault (phase A to ground fault) impedance, fault resistance, per unit length, positive sequence line impedance, relay faulted phase current, grid faulted phase current, transformer zero sequence current and $k = \frac{Z_L^0 - Z_L^1}{3Z_L^1}$ respectively. In (5.25), the component $\frac{(Res_F + pZ_L^1)I_{R_1}^a}{I_{R_1}^a + 3kI_{tr}^0}$ highlights dependence of the apparent impedance on the converter side current (remotely contributed from bus 2), which is limited by 1.15-1.2 pu (saturation limit). The denominator part of (5.25) ($I_{R_1}^a + 3kI_{tr}^0$) further dominated by positive sequence converter current (remote contribution) component ($\leq 1.5 - 1.2$ pu), negative sequence component contribution from converter is suppressed to zero to de-stress IGBTs, which further influence the apparent impedance trajectory seen by the relay R_1.

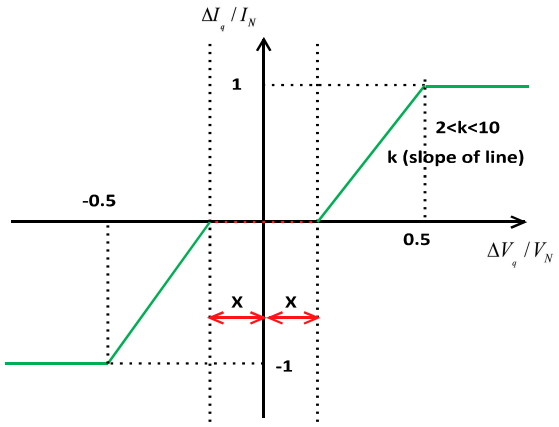

Figure 5.8: LVRT control characteristics of MMC controller

The detailed description of LVRT control characteristic could be explained from Fig 5.8. The additional converter reactive current (ΔI_q) support should be directly proportional to the voltage drop (ΔV) at the PCC, expressed as $\Delta I_q = k \times \Delta V/V$, where the reactive current droop (k) can be adjusted within a range of 2-10 pu. To achieve this, voltage control is initiated within 20 ms of detecting a fault if the network voltage deviates by more than 10 % (X) from the its root mean square (rms) value, which creates a dead band of $\pm$0.1 pu as shown in Fig. 5.8 [140]. Furthermore, this voltage support is maintained throughout the fault duration even after the voltage returns to the dead band.

At 0.2 s, a LG fault F_2 is simulated for 400 ms at a distance of 5 km from AC bus 2 in OHTL L_{12AC} of test hybrid AC/DC grid shown in Fig. 5.4, which lies in zone-2 for conventional mho relay R_1 located at bus 6 in test system. The LVRT controller of MMC converter 2 will get activated, when PCC voltage (Bus 2) falls below the threshold voltage (0.9 pu in test system) set by the grid code, during fault and it will support the converter bus (Bus 2) voltage by injecting reactive power as shown in Fig. 5.9(a). The grid bus (Bus 3) also contribute reactive power to the system as shown in Fig. 5.9(a). The active power support from MMC 2 drops down to zero during fault as shown in Fig. 5.9(b). The DC current and voltage response to the AC fault F_2 is shown in Fig.5.9(g) and (h), which shows the recovery of HVDC grid after the fault event clearance. The apparent impedance (Z_{app}) trajectory for LG fault F_2 in the test hybrid AC/DC system, with and without HVDC, is plotted for mho relay R_1 in Fig.5.9(i). As evident form Fig.5.9(i), the mho relay correctly identifies the fault F_2 in zone-2 for test system without MMC

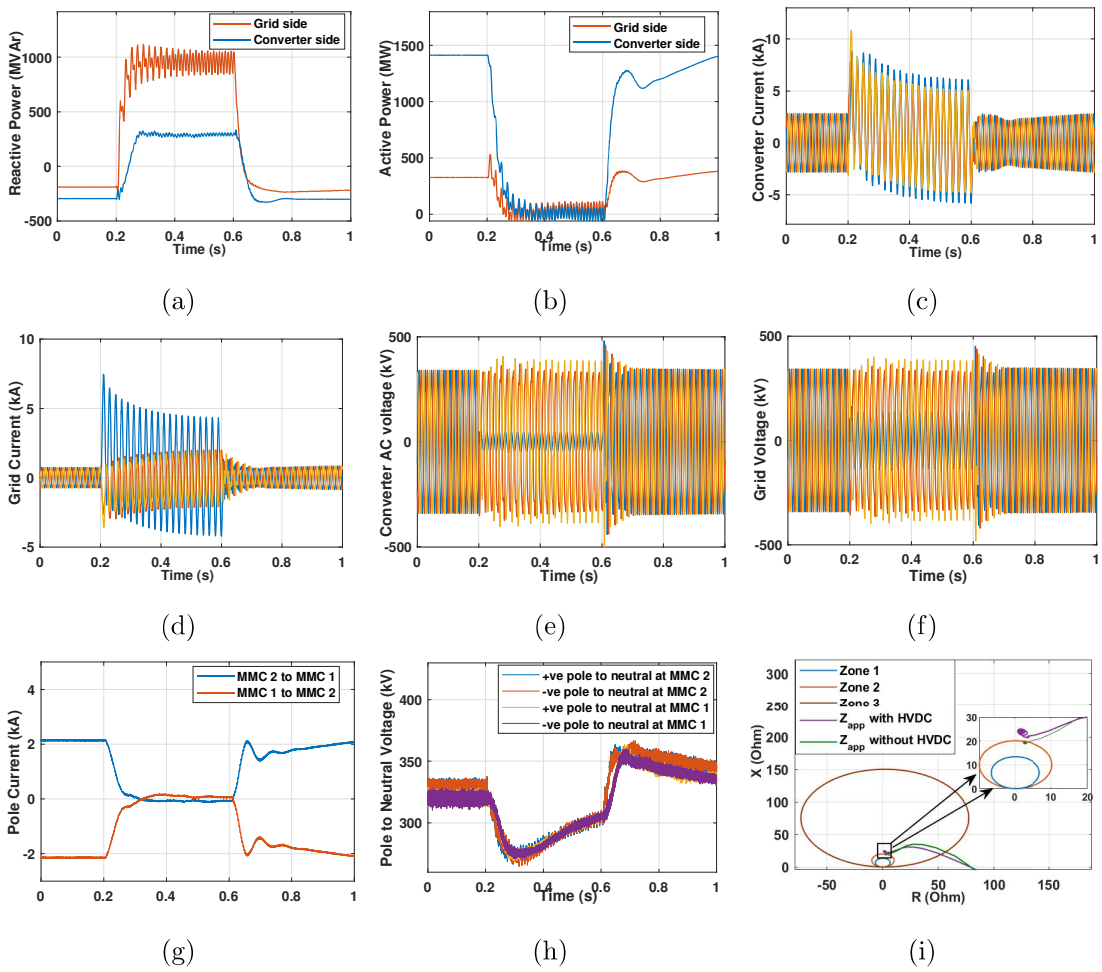

Figure 5.9: Impact of LVRT control on conventional distance protection scheme (a) Reactive power flow from MMC 2 & L_{23} from bus 3, (b) Active power flow from MMC 2 & L_{23} at bus 3, (c) Current contribution from MMC 2, (d) Current contribution from L_{23} at bus 3, (e) AC voltage at MMC 2, (f) AC voltage at bus 3, (g) DC current in HVDC link, (h) DC pole voltage at MMC 1 and MMC 2 terminal, (i) Z_{app} seen by Relay R_1 with and without HVDC LVRT controller

based HVDC system, whereas the mho relay classifies the fault F_2 as zone-3 fault which highlights the underreach issue with conventional mho relay.

The fast SMPA based TWAT information at all DFRs are tabulated in Table 5.7 for fault F_2 with different combination of fault type and fault location in OHTL L_{12AC} and cable L_{23}. After that (5.24) and (5.22) of the graph theory based wide area real time fault location is used to locate fault as tabulated in Table 5.7, which correctly identifies the zone of intended fault that will help in secured backup protection of the hybrid AC/DC

Table 5.7: Performance of WABPS against LVRT control in MMC converter for fault in L_{12AC} and L_{23}.

Fault type & distance (km)	TWAT at DFR location							Fault zone	FLE (%)
	DFR A	DFR B	DFR C	DFR D	DFR E	DFR F	DFR G		
LG & 5 in L_{12AC}	0.201113833	0.2000250543	0.200156934	0.200298603	0.2008618535	0.2008575462	0.20071951886	Zone-2	0.202
LL & 5 in in L_{12AC}	0.20111226732	0.2000224826	0.2001573026	0.200299584	0.200860367	0.200855726	0.200720761	Zone-2	0.184
LG & 20 in L_{12AC}	0.2010718507	0.2000618532	0.2002017943	0.2003358594	0.2008995820	0.2009036834	0.2006196324	Zone-3	0.138
LG & 10 in L_{23}	0.2012124972	0.2000837823	0.20022748261	0.2003661025	0.2009285390	0.700931539	0.70078839255	Zone-2	0.152
LL & 30 in in L_{23}	0.201376448	0.2002482154	0.2003859273	0.2003610250	0.2009247371	0.2009216340	0.2009519543	Zone-3	0.140

transmission system.

5.5 Summary

In this chapter, a robust and secured TW based WABPS is designed for mixed cable and OHTL of the HVAC grid interfacing MMC converter based HVDC link. A fast SMPA algorithm is used to estimate TWAT in DFR located at the AC bus terminal using low sampling frequency (50 kHz) measurement and sent to WABPC via dedicated communication channel conforming to IEC-61850 communication protocol. A graph theory based wide area real time fault location is estimated and a distance protection based supervisory backup trip signal is sent to the associated circuit breaker in the HVAC grid. The performance of proposed WABPS is validated against fault types, fault resistance, fault distance and LVRT control of MMC converter, and its application could also be extended for wide area real time fault localization in the HVAC transmission network.